Numerical Study of the Effect of Viscous Heat Dissipation and Compression Work on Microscale Rayleigh–Bénard Convection Based on a Coupled Thermal Lattice Boltzmann Method

X Ren, F Liu, S Wang, S Wei*
Shandong University, China

ABSTRACT

In the present work, an improved double-distribution-function thermal lattice Boltzmann method (LBM) is developed for analyzing the effect of viscous heat dissipation and compression work on microscale Rayleigh–Bénard convection. In the proposed method a temperature change is introduced into the LB momentum equation in the form of a momentum source to realize the coupling between the momentum and the energy fields; two sets of evolution equations are established, one for the mass and momentum conservation and the other for the total energy that incorporates viscous heat dissipation and compression work. Numerical results show that the effect of viscous heat dissipation and compression work on the temperature distribution, flow distribution, and average Nusselt number at some Rayleigh numbers and aspect ratios is significant.

1. INTRODUCTION

Rayleigh–Bénard convection [1] is a thermally induced flow between two horizontal plates that are heated from below. As one of benchmark problems of hydrodynamic instability, Rayleigh–Bénard convection is of considerable scientific and engineering importance. Moreover, Rayleigh–Bénard convection involves in various technological applications such as nuclear reactor insulation, solar collectors, crystal growth in liquids, heat exchangers, and cooling of electronic equipment, and particularly the cooling of electronic circuits in microelectromechanical systems [2]. Therefore, much effort has been spent on investigating Rayleigh–Bénard convection. Zhou et al. studied the geometric and physical properties of thermal plumes in turbulent Rayleigh–Bénard convection [3]. A high-resolution measurement of the velocity and temperature boundary layers in Rayleigh–Bénard convection was conducted by Sun et al. with applying the particle image velocimetry technique [4]. Sharif and Mohammad investigated the natural convection within cavities with different inclination angles and cavity aspect ratios [5]. Valencia et al. measured the velocity field and time-averaged flow structures in a cubical cavity that was heated from below and cooled from above [6]. Kao et al. investigated the nonlinear phenomena of two-dimensional (2D) natural convection in enclosed rectangular cavities and systematically examined the relationship

*Corresponding Author: sswei@sdu.edu.cn

between the Nusselt number (Nu) and the reference Rayleigh number (Ra) [7]. Chakraborty and Chatterjee studied the Rayleigh–Bénard convection occurring in directional solidification by using a novel hybrid lattice Boltzmann method (LBM) [8].

The aforementioned investigations showed that the formation of flow structures due to Rayleigh–Bénard convection are affected by the boundary conditions, aspect ratio of the cavity, and direction of the gravitational effect. However, few of the studies, except that presented in [9], have considered the effect of viscous heat dissipation and compression work on microscale Rayleigh–Bénard convection. In the model developed in Ref. 9 the temperature equilibrium distribution function always takes negative values, and this model is more complicated than other double-distribution-function (DDF) models, even when the viscous heat dissipation and compression work are negligible.

With a decrease of the system size, the effect of viscous dissipation [10] and compression work [11,12] on the thermal and hydrodynamic behavior is more significant and should not be neglected [13].

The kinetic-based LBM [14], due to its advantages, such as high computational efficiency, easy implementation, and use of parallel algorithms, has become a powerful numerical technique for simulating fluid flows and modeling the physics of fluids [15,16,17]. Various thermal LB models or Boltzmann-based schemes have been employed to investigate natural convection problems [18,19,20]. The multispeed LBM is a straightforward extension of the isothermal LBM; however, it usually suffers from severe numerical instability, and the simulation of the temperature variation is limited to a narrow range [21]. In the hybrid LBM, the flow simulation is performed by using the LBM; however, the energy equation is solved through conventional numerical methods. Therefore, this method has not demonstrated the advantages of the standard LBM [19]. The DDF-LBM uses two distribution functions, one for the velocity field and the other for the temperature or internal energy field. And it takes into account the viscous heat dissipation and compression work [22,23]. However, most of the DDF-LBM models are decoupling models in the sense that the change of temperature cannot influence the velocity field [14]. Hence, the decoupling models are only applicable to Boussinesq flows in which the temperature variation is minor. When these models are applied to the thermal problems in which the temperature field has significant effects on the flow field, the decoupling between the momentum and the energy transports causes considerable errors. To overcome this problem, on the basis of the total energy DDF-LBM [24], we attempt to propose a coupled DDF thermal LBM (coupled DDF-TLBM) [25] that incorporates viscous heat dissipation and compression work. In order to realize the coupling between the momentum and the energy fields, this method introduces the temperature change into the LB momentum equation in the form of a momentum source, which affects the distribution of flow velocity and density. Although numerous studies have demonstrated the capabilities of LB models in simulating natural convection, an appropriate model for reflecting the effect of viscous heat dissipation and compression work is still desirable for microscale Rayleigh–Bénard convection without the Boussinesq approximation.

2. METHODS

2.1 The Microscale Rayleigh–Bénard Convection

As shown in figure 1, the microscale Rayleigh–Bénard convection occurs in a 2D rectangular cavity with thermally insulated sidewalls filled with a viscous incompressible static fluid with an initial temperature T0. The temperatures of the top and bottom plates

are constant but different. Specifically the top plate is cold with a temperature Tc, and the bottom plate is hot with a temperature Th. The height, width and aspect ratio of the rectangular cavity are denoted as H, L and A with A=H / L.

The Ra [26] and Prandlt number (Pr) [27] are dimensionless parameters that are associated with Rayleigh–Bénard convection flow. Ra is the ratio of buoyancy to viscosity forces multiplied by the ratio of momentum to thermal diffusivities. It characterizes the transition between the conduction- and convection-dominated flows. Pr is the ratio of viscous diffusion to thermal diffusion.

$$Pr = \mu c_p / \kappa \tag{1}$$

$$Ra = \frac{\rho g \beta (T_h - T_c) L^3 Pr}{\mu^2} \tag{2}$$

where c_p is the specific heat coefficient at constant pressure, $c_p=(D+2)R/2$ with D being the spatial dimension and R the gas constant, g is the acceleration of gravity, β is the isobaric coefficient of thermal expansion, μ is the dynamic viscosity, κ is the thermal conductivity, and ρ is the fluid density.

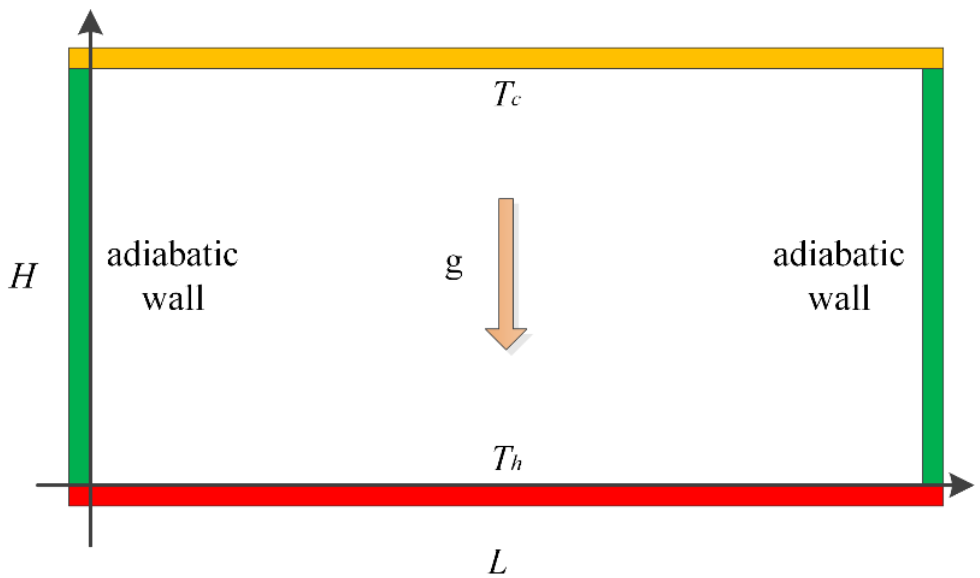

Figure 1: Diagram of microscale Rayleigh–Bénard convection

2.2 The Coupled DDF-TLBM

In 2007, Guo et al. [24] proposed the decoupling DDF-TLBM to solve low Mach number thermal flow with viscous dissipation and compression. The decoupling DDF-TLBM consists

of two sets of evolution equations: one for the mass and momentum conservation, and the other for the total energy that incorporates viscous heat dissipation and compression work. The evolution equations can be written as follows:

$$f_i(\boldsymbol{x}+\boldsymbol{e}_i\Delta t, t+\Delta t) = f_i(\boldsymbol{x},t) - \frac{1}{\tau_f}[f_i(\boldsymbol{x},t) - f_i^{eq}(\boldsymbol{x},t)] + \delta_t(1-\frac{w_f}{2})\cdot F_i \tag{3}$$

$$\begin{aligned} h_i(\boldsymbol{x}+\boldsymbol{e}_i\Delta t, t+\Delta t) &= h_i(\boldsymbol{x},t) - w_h[h_i(\boldsymbol{x},t) - h_i^{eq}(\boldsymbol{x},t)] \\ &+(w_h - w_f)[f_i(\boldsymbol{x},t) - f_i^{eq}(\boldsymbol{x},t) + \frac{\delta_t}{2}F_i](\boldsymbol{e}_i\cdot\boldsymbol{u} - \frac{\boldsymbol{u}^2}{2}) + \delta_t(1-\frac{w_h}{2})q_i \end{aligned} \tag{4}$$

where x is the position of the lattice node; δt is the time step; $w_f = 2\delta_t/(2\tau_f + \delta_t)$, $w_h = 2\delta_t/(2\tau_h + \delta_t)$, where τ_f and τ_h are the dimensionless relaxation times for momentum and total energy, respectively; f_i and h_i are respectively the density distribution function and total energy distribution function; f_i^{eq} and h_i^{eq} are the equilibrium distribution functions; $\boldsymbol{e}_i$ and u are the discrete velocities of the fluid particles and macroscopic velocity, respectively; and F_i and q_i are two terms related to the external force:

$$F_i = \omega_i\rho[\frac{\boldsymbol{e}_i\cdot\boldsymbol{a}}{RT_0} + \frac{(\boldsymbol{e}_i\cdot\boldsymbol{u})(\boldsymbol{e}_i\cdot\boldsymbol{a})}{R^2T_0^2} - \frac{\boldsymbol{a}\cdot\boldsymbol{u}}{RT_0}] \tag{5}$$

$$q_i = [\omega_i\frac{\rho E}{RT_0} + f_i^{eq} + (1-\frac{w_f}{2})(f_i - f_i^{eq} + \frac{\delta_t}{2}F_i)]\boldsymbol{e}_i\cdot\boldsymbol{a} \tag{6}$$

where a is the external force acceleration, $a_x = 0, a_y = -\rho g$ for the microscale Rayleigh–Bénard convection model, T0 is the reference temperature ($T_0 = (T_h + T_c)/2$ for the Rayleigh-Bénard convection model). In the following we use the D2Q9 lattice model. Thus the local fluid density and energy equilibrium distribution functions and the discrete velocities of the fluid particles $\boldsymbol{e}_i$ are given by

$$f_i^{eq}(T_0) = \rho\omega_i[1 + \frac{\boldsymbol{e}_i\cdot\boldsymbol{u}}{RT_0} + \frac{1}{2}(\frac{\boldsymbol{e}_i\cdot\boldsymbol{u}}{RT_0})^2 - \frac{\boldsymbol{u}^2}{2RT_0}] \tag{7}$$

$$h_i^{eq}(T_0) = Ef_i^{eq} + \omega_i p_0[\frac{\boldsymbol{e}_i\cdot\boldsymbol{u}}{RT_0} + (\frac{\boldsymbol{e}_i\cdot\boldsymbol{u}}{RT_0})^2 - \frac{\boldsymbol{u}^2}{RT_0} + \frac{1}{2}(\frac{\boldsymbol{e}_i^2}{RT_0} - D)] \tag{8}$$

$$\boldsymbol{e}_i = \begin{cases} 0 & i = 0 \\ (\cos[\frac{\pi(i-1)}{2}], \sin[\frac{\pi(i-1)}{2}])c & i = 1,2,3,4 \\ \sqrt{2}(\cos[\frac{\pi(i-9/2)}{2}], \sin[\frac{\pi(i-9/2)}{2}])c & i = 5,6,7,8 \end{cases} \tag{9}$$

where $c = \sqrt{3RT_0}$ is the particle streaming speed, $p_0 = \rho RT_0$, ω_i is the weighting factor for the various lattice links, and $\omega_0 = 4/9$, $\omega_1 = \omega_2 = \omega_3 = \omega_4 = 1/9$, $\omega_5 = \omega_6 = \omega_7 = \omega_8 = 1/36$.

According to the conservation of the collision operator, the macroscopic variable velocity and total energy are directly calculated by using the distribution functions:

$$\boldsymbol{u} = \frac{\sum_i \boldsymbol{e}_i f_i}{\sum_i f_i} + \frac{\delta_t}{2}\boldsymbol{a}, \quad E = \frac{\sum_i h_i}{\sum_i f_i} + \frac{\delta_t}{2}\boldsymbol{u}\cdot\boldsymbol{a} \tag{10}$$

Through a Chapman-Enskog analysis, it is found that the pressure p0 is the dynamic pressure rather than the thermodynamic pressure, and the change of the temperature field cannot influence the velocity field [24].

In order to realize the coupling between the momentum field and energy field, the coupled DDF-TLBM presented in this paper introduces the temperature change into the LB momentum equation in the form of the momentum source Ki, which affects the distribution of flow velocity and density. It is form of

$$f_i(\boldsymbol{x} + \boldsymbol{e}_i\Delta t, t + \Delta t) = f_i(\boldsymbol{x}, t) - \frac{1}{\tau_f}[f_i(\boldsymbol{x}, t) - f_i^{eq}(\boldsymbol{x}, t)] + \delta_t(1 - \frac{w_f}{2})\cdot F_i + \delta_t\omega_i K_i \tag{11}$$

In accordance with the definition of the total energy $E = c_v T + \boldsymbol{u}^2/2$, where $c_v = DR/2$ is the specific heat at constant volume, the temperature T at the lattice x and moment t is given by

$$T(\boldsymbol{x}, t) = \frac{1}{c_v}(\sum_{i=0}^{8} h_i(\boldsymbol{x}, t) / \rho(\boldsymbol{x}, t) - \frac{1}{2}\boldsymbol{u}(\boldsymbol{x}, t)^2) \tag{12}$$

The temperature difference $T_i(\boldsymbol{x}, t)$ between the lattice x and the surrounding lattice point in the direction $\boldsymbol{e}_i$ is given by

$$T_i(\boldsymbol{x}, t) = T(\boldsymbol{x}, t) - T(\boldsymbol{x} + \boldsymbol{e}_i\Delta t, t) \tag{13}$$

The momentum source K_i produced by the temperature change is written as follows:

$$K_i = (\frac{\boldsymbol{e}_i \cdot \boldsymbol{u}}{R^2 T_0^2} - D)(\frac{T(\boldsymbol{x},t)}{T(\boldsymbol{x},t+\delta_t)} - 1) + \frac{\boldsymbol{e}_i \cdot \boldsymbol{u}}{2RT_0}(\frac{\boldsymbol{e}_i^2}{RT_0} - D - 2)T_i(\boldsymbol{x},t) \tag{14}$$

The temperature change in K_i includes two parts: one for the same lattice at different times that affects the thermal diffusion coefficient and viscosity coefficient of the fluid; and the other for different lattices at same time that affects the velocity distribution of the flow field. The temperature change is introduced into the LB equation in the form of the momentum source and influences the flow field through collision and migration. This coupled DDF-TLBM can realize the coupling between the momentum field and energy field, and overcome the limitation of the Boussinesq approximation. Hence it extends the application range of the thermal LBM. τ_f and τ_h are expressed by the dimensionless characteristic parameters Pr, Ra, and Mach number (Ma) ($Ma = u_c / c_s$ with $u_c = \sqrt{g\beta\Delta TH}$, $c_s = \sqrt{RT_0}$), that is

$$\tau_f = \frac{MaH\sqrt{Pr}}{\sqrt{RaRT_0}}, \quad \tau_h = \frac{MaH}{\sqrt{RaRT_0 Pr}} \tag{15}$$

In practical applications, the flow boundary conditions are usually specified in terms of the fluid variables. The nonequilibrium-extrapolation approach [24] is employed to transform thermos-hydrodynamic boundary conditions to the boundary conditions of the distribution functions due to its simplicity, second-order accuracy, and good robustness. In this method, the distribution function at a boundary node is separated into the equilibrium and nonequilibrium components. The equilibrium component is determined by using the macroscopic variables of the boundary, and the nonequilibrium component is identified by using the distribution function at the nearest node in the fluid region [14]. According to this approach, the density and energy distribution function at a boundary node x_b can be expressed as

$$f_i(x_b,t) = f_i^{eq}(x_b, \rho_b, \boldsymbol{u}_b, t) + \left[f_i(x_f,t) - f_i^{eq}(x_f,t) \right] \tag{16}$$

$$h_i(x_b,t) = h_i^{eq}(x_b, E_b, \boldsymbol{u}_b, t) + \left[h_i(x_f,t) - h_i^{eq}(x_f,t) \right] \tag{17}$$

where $\boldsymbol{x}_f$ is the nearest fluid neighborhood, $f_i^{eq}(x_b, \rho_b, \boldsymbol{u}_b, t)$ and $h_i^{eq}(x_b, E_b, \boldsymbol{u}_b, t)$ are determined by the values of the macroscopic variables at the boundary,

and $\boldsymbol{u}_b = (0,0)$, $\rho_b = \rho(\boldsymbol{x}_f)$, $E_b = c_v T_b + \frac{\boldsymbol{u}_b^2}{2}$, $T_b = \begin{cases} T(\boldsymbol{x}_f) & \text{for adiabatic wall} \\ T_c & \text{for top plate} \\ T_h & \text{for bottom plate} \end{cases}$.

The aforementioned equations constitute the coupled DDF-TLBM that incorporates viscous heat dissipation and compression work. For the flow model without the viscous heat dissipation and compression work, an internal energy distribution function g_i is used in the temperature field, and the evolution equation is expressed as follows:

$$g_i(\boldsymbol{x}+\boldsymbol{e}_i\Delta t, t+\Delta t) = g_i(\boldsymbol{x},t) - w_g[g_i(\boldsymbol{x},t) - g_i^{eq}(\boldsymbol{x},t)] \tag{18}$$

where the internal equilibrium distribution functions $g_i^{eq}(\boldsymbol{x},t)=DRT_0 f_i^{eq}(\boldsymbol{x},t)/2$, $w_g = 2\delta_t/(2\tau_g+\delta_t)$, and $\tau_g = \kappa/pc_p$.

3. RESULTS AND DISCUSSION

By using the method discussed above, two models will be employed to describe the Rayleigh–Bénard convection. One considers the viscous heat dissipation and compression work (model I) and the other does not take into account the viscous heat dissipation and compression work (model II). The numerical-simulation experiments are conducted to investigate the effect of the viscous heat dissipation and compression work on the temperature distribution, flow distribution, and average Nu [28] for various values of the parameters, such as Ra and the aspect ratio A. In the computations 128×64 lattices is employed to divide the flow domain (128μm×64μm). Table 1 lists the default values of the parameters used in the simulations.

Table 1. Default Values of the Basic Parameter Variables Used in the Simulations

Parameters	Value
H	64 (μm)
L	128 (μm)
A	1/2
Tc	305(K)
Th	315(K)
Pr	0.7
Ra	105
Ma	0.1

3.1 Impact of Ra on the Flow Field and Temperature Distribution

Figure 2 shows the velocity profiles of the flow field at a steady state for Ra = 10^3, 10^4, 10^5, and 10^6 where figure 2 (a1)–(a4) is for the mode I and figure 2 (b1)–(b4) for the model Π. Figure 3 displays the isotherms corresponding to the velocity profiles.

As shown in figures 2 and 3, when Ra = 10^3, the heat conduction plays a crucial role in the two models, and the convection effect is weak. The effect of the viscous heat dissipation and compression work is minor. Consequently, the velocity profiles and isotherms of the two models are similar. When Ra = 10^4, the convection effect is enhanced, and the effect of the viscous heat dissipation and compression work becomes apparent. Therefore, the differences between the two models are evident. The velocity profile in figure 2 (a2) has larger vortexes and a clearer boundary than that in figure 2 (b2). Figure 3 (a2) and (b2) illustrates the differences in temperature distribution. When Ra = 10^5, the differences between the two

models are significant. In figure 2 (a3), the shape of the vortex is upside down. The convective heat transfer plays a crucial role in the model I. For the model Π, the role of heat conduction is the same as that of thermal convection. When Ra = 10^6, the convection heat transfer plays a dominant role in both models; however, the model I has clearer velocity and temperature boundary layers.

This result shows that the effect of the viscous heat dissipation and compression work can promote convection heat transfer, which considerably affects the velocity and thermal distribution of microscale Rayleigh–Bénard convection.

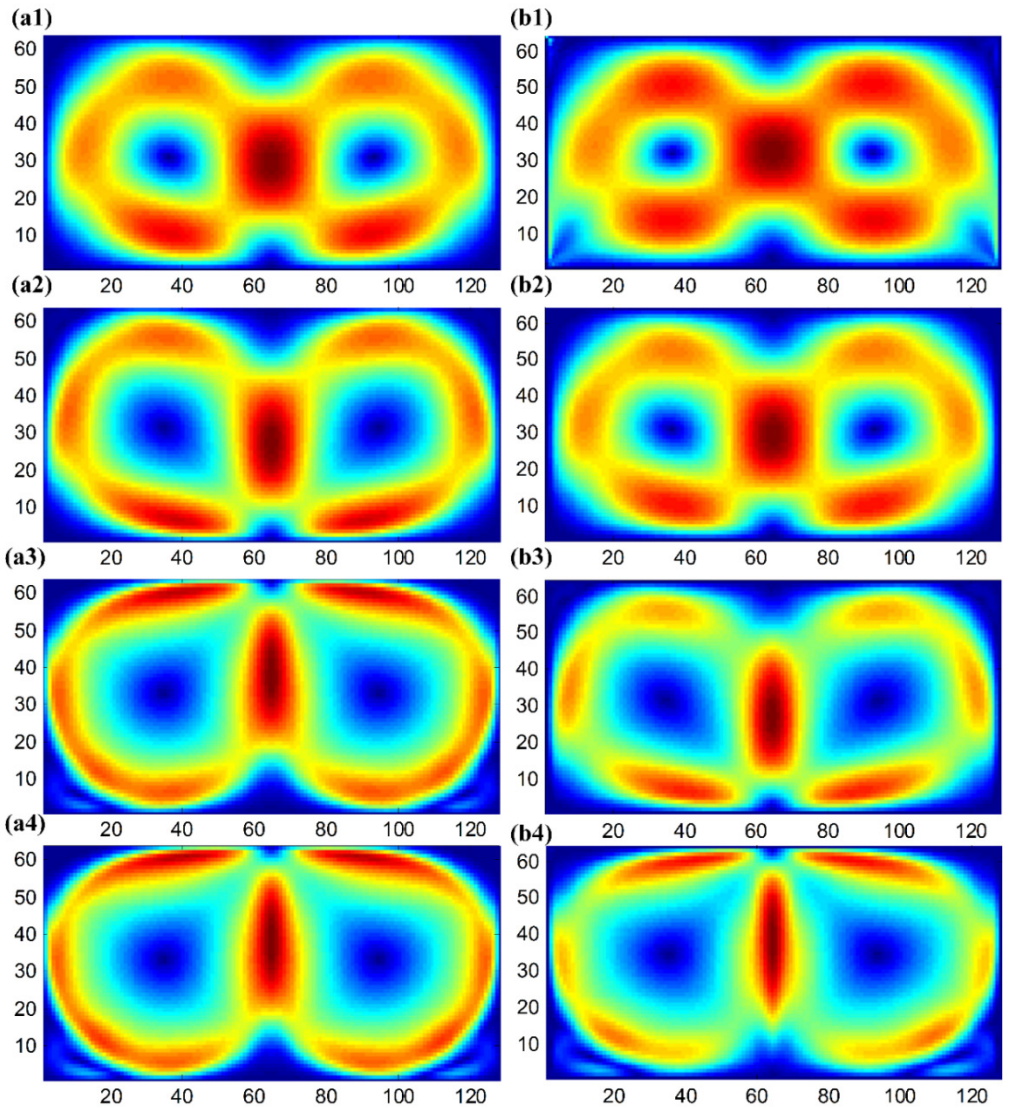

Figure 2: Velocity profiles: ((a1)–(a4)) for the model I; ((b1)–(b4)) for the model Π with Ra = 10^3, 10^4, 10^5, and 10^6, respectively

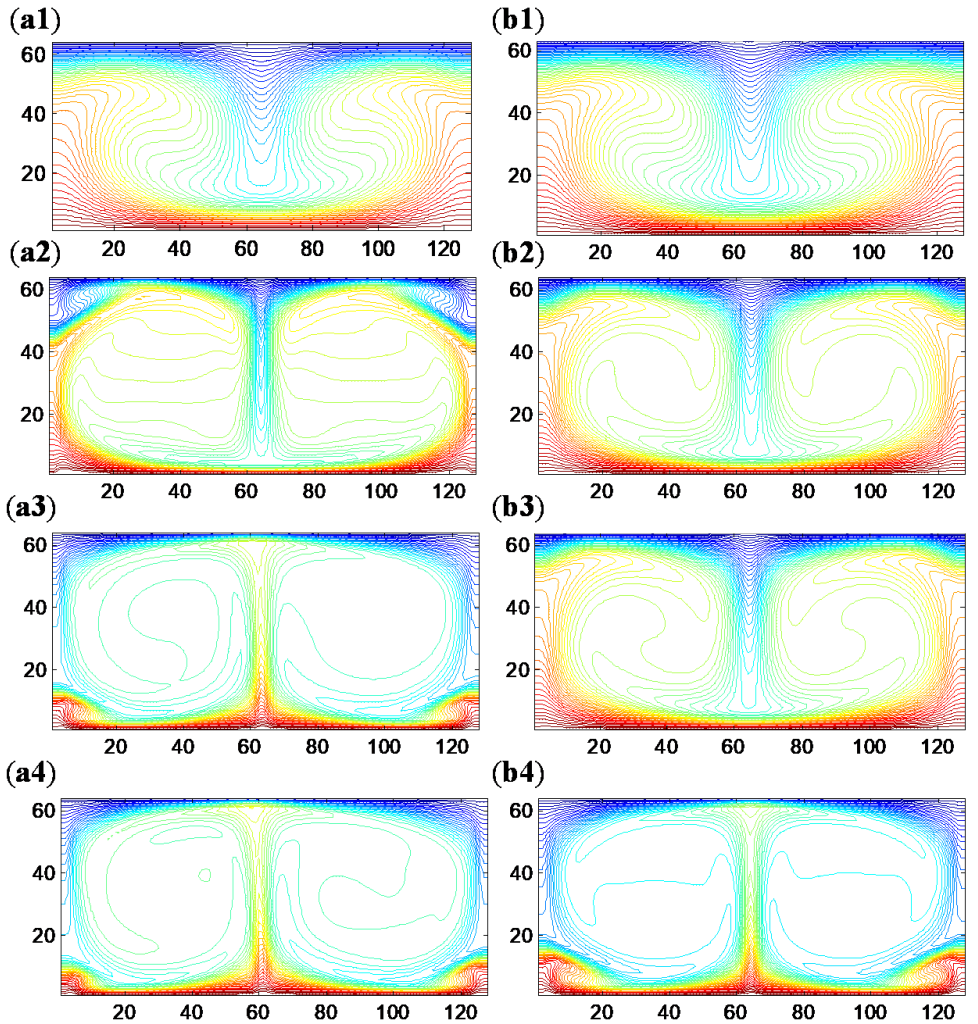

Figure 3: Isothermal diagrams: ((a1)–(a4)) for the model I; ((b1)–(b4)) for the model II for Ra = 10^3, 10^4, 10^5, and 10^6, respectively

In heat transfer at a boundary (surface) within a fluid, Nu is the ratio of convective to conductive heat transfer across (normal to) the boundary. When the Nu is higher, the effect of the convective heat is more evident. To further explore the effect of viscous heat dissipation and compression work, Table 2 lists the average values of Nu ($\overline{Nu}$) of the two models for various values of Ra, which are calculated as follows:

$$\overline{Nu} = \frac{1}{H}\int_0^H Nu\,\mathrm{d}y = -\frac{1}{H}\int_0^H \left(\frac{\partial T}{\partial x}\right)\mathrm{d}y \tag{19}$$

As shown in Table 2, $\overline{Nu}$ increases with the increase of Ra. The total amount of heat transferring to the cold wall from the hot wall is increased; in other words, the convection resistance decreases, and the thermal conductivity resistance increases. For the same Ra number, $\overline{Nu}$ of the model I is higher than that of the model Π. This suggests that the viscous heat dissipation and compression work enhances the convective heat transfer. Therefore, the effect of viscous heat dissipation and compression work is crucial to Rayleigh–Bénard convection and should not be ignored.

Table 2: $\overline{Nu}$ of the Two Numerical Models for Various Values of Ra

Ra	$\overline{Nu}$	
	model I	**model Π**
103	1.7121	1.2562
104	4.6522	2.4536
105	8.5368	5.1989
106	14.374	9.465

3.2 Impact of Aspect Ratios (A) on the Flow Field and Temperature Distribution Temperature Distribution

Next consider the effect of viscous heat dissipation and compression work on the flow field and temperature distribution of the microscale Rayleigh–Bénard convection with different geometries. With the length fixed, the height of the flow domain is adjusted to obtain different aspect ratios (A). Figure 4 shows the velocity distribution profiles of the flow field at a steady state for A = 1, 1/2, 1/3, 1/4, 1/5, and 1/6. Figure 4 (a1)–(a6) is for the velocity distribution profiles of the mode I, and figure 4 (b1)–(b6) for the velocity distribution profiles of the model Π. Figure 5 displays the corresponding isotherm diagrams.

From figure 4 one can see that when A = 1, the velocity distributions and isotherms of the two models are similar. For the velocity field, a large eddy is formed in the square cavity. Note that the eddy of the model I is more intense than that of the model Π. The case for A = 1/2 has been discussed in Sect. 3.1. The decrease in the system size enhances the effect of viscous heat dissipation and compression work. When A = 1/3, 1/4, 1/5, and 1/6, the differences between the two models are clearer. For the model Π, when A = 1/3, 1/4, 1/5, and 1/6 there are 3, 4, 5, and 6 eddies, respectively; in other words, the number of vortexes is inversely proportional to the aspect ratio A. By contrast, for the model I, when A = 1/3, 1/4, 1/5, and 1/6 there are 4, 6, 8, and 10 eddies, respectively. From figure 5, the similar phenomena are observed in the isothermal diagrams. As the aspect ratio decreases, the size of the flow domain decreases, and the effect of the viscous heat dissipation and compression work increases; the number of eddies increases linearly, and their shape is also changed. For the model Π, the eddies are elliptical, and the long axis of the eddies is tilted. For the model I, the long axis of the elliptical spiral is vertical. Therefore, the effect of viscous heat dissipation and compression work should be considered for the microscale flow.

The temperature profiles along the height of cavity for $Ra=10^4$ and A=1 are shown in figure 6. The blue lines are for the result obtained based on the model I and the red lines for the model Π. Figure 6 shows that the temperature gradient near the wall is large and the

temperature change becomes smooth in the middle region, and the smooth region of model I is larger than that of model Π. Therefore, the convection effect is significant in the model Π due to the viscous heat dissipation and compression work.

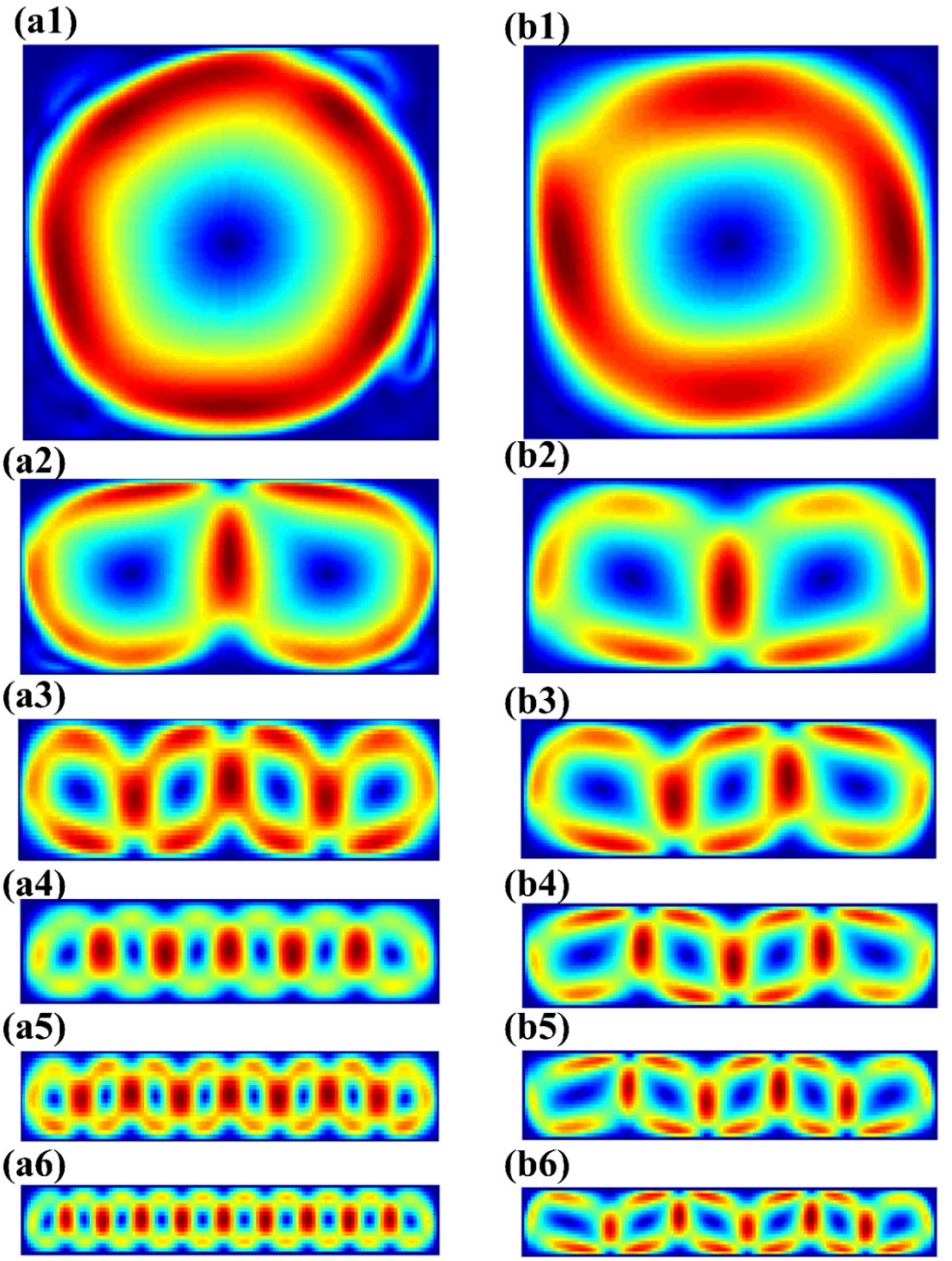

Figure 4: Velocity distribution Profiles ((a1)–(a6)) of the model I and those ((b1)–(b6)) of the model Π for A = 1, 1/2, 1/3, 1/4, 1/5, and 1/6, respectively

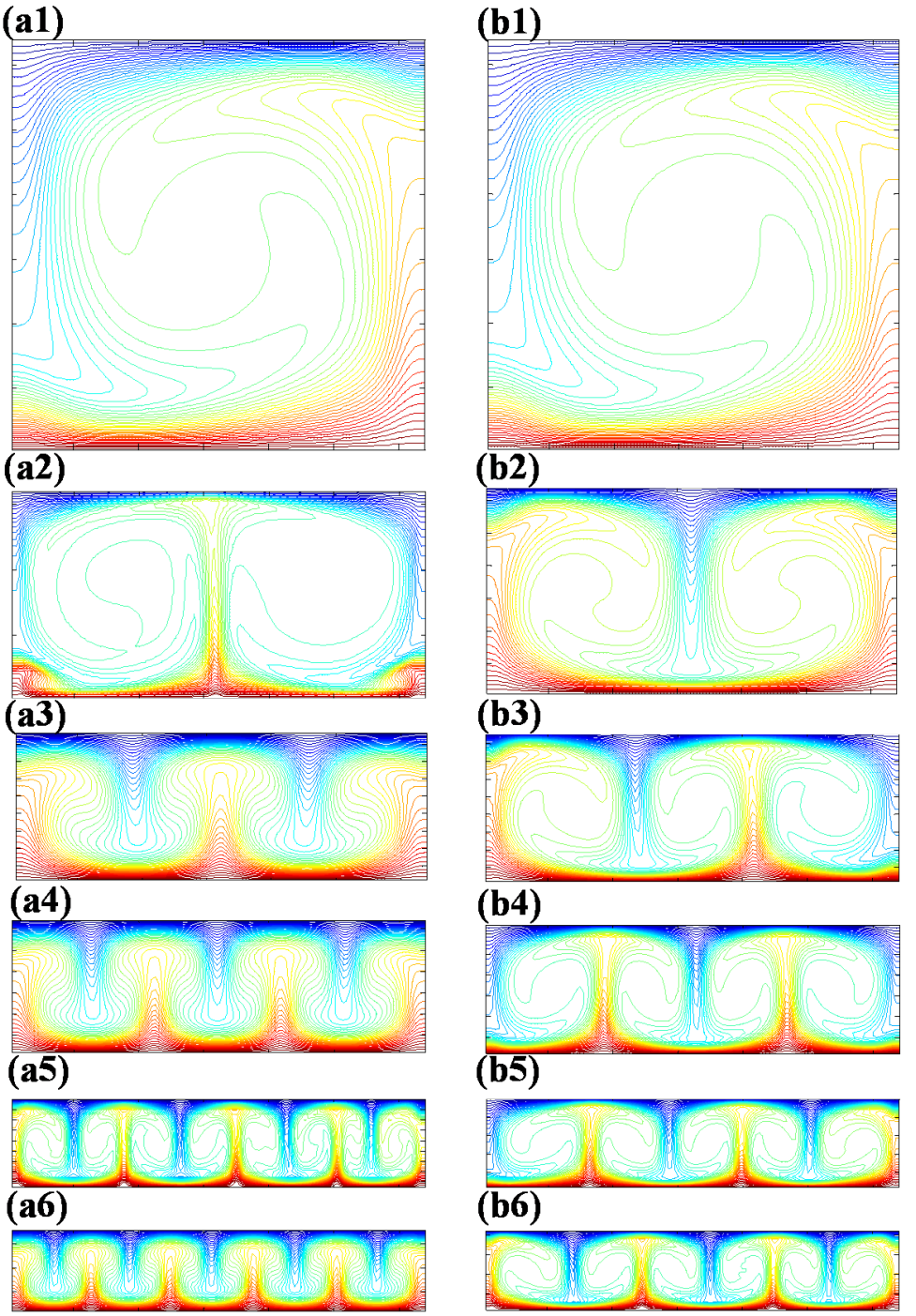

Figure 5: Isothermal diagrams ((a1)–(a6)) of the model I and those ((b1)–(b6)) of the model II for A = 1, 1/2, 1/3, 1/4, 1/5, 1/6, respectively

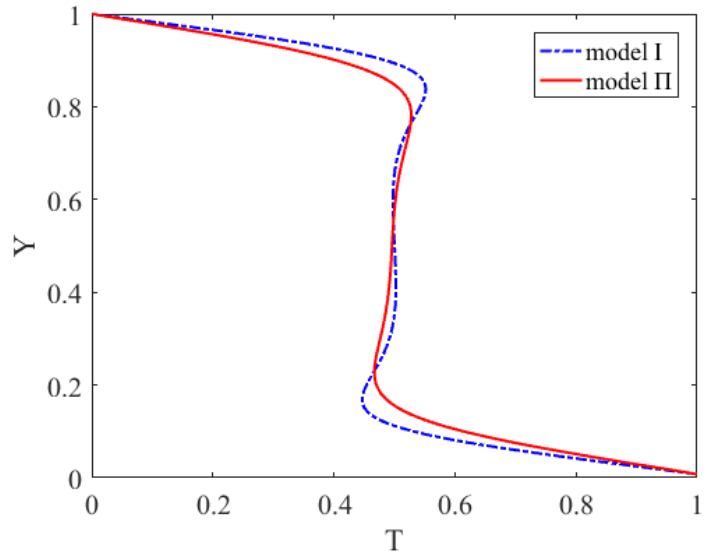

Figure 6: The normalized temperature profiles along the height of the cavity at Ra=10^4 and A=1, the blue line denotes the model I and the red line denotes the model Π

Figure 7 illustrates the relationship between the $\overline{Nu}$ and the aspect ratio (A); the blue □ line denotes the model I, and the green ○ line denotes the model Π. As the aspect ratio (A) decreases, the average number increases. However, the growth trends of the two models are different. For the model Π, the $\overline{Nu}$ increases more slowly than that of the model I.

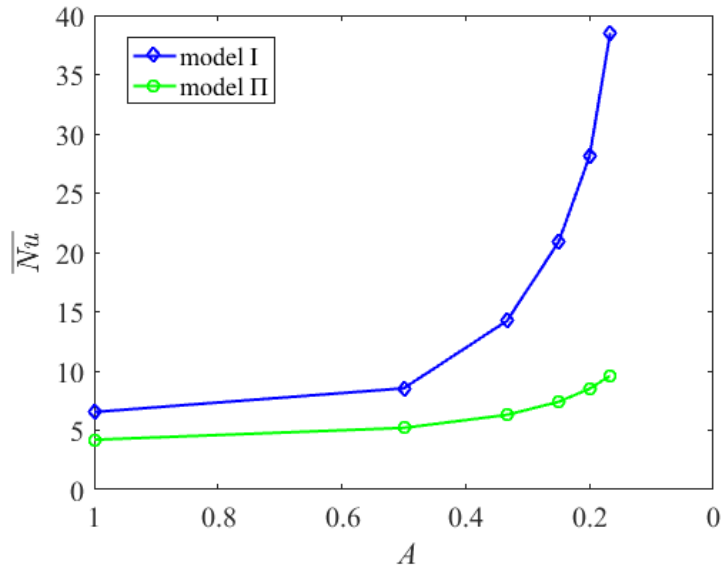

Figure 7: Relationship between the average Nu ($\overline{Nu}$) and the aspect Ratio (A); the blue □ line denotes the model I, and the green ○ line denotes the model Π

4. CONCLUSIONS

In order to investigate the effect of viscous heat dissipation and compression work, the coupled DDF-TLBM is applied to two microscale Rayleigh–Bénard convection numerical models, one considering the viscous heat dissipation and compression work and the other not considering the viscous heat dissipation and compression work. The numerical-simulation experiments were conducted to study the effect of the viscous heat dissipation and compression work on the temperature distribution, flow distribution, and average Nu at different values of Ra and aspect ratios (A). It is found that when Ra > 104, the effect of viscous heat dissipation and compression work promote the convection heat transfer and have a profound effect on the Rayleigh–Bénard convection model; as the size of the flow domain decreases, the number of eddies increases linearly and their shape is also changed in the model that takes into account the viscous heat dissipation and compression work.

This study demonstrated that the coupled DDF-TLBM can provide a new sight for the microscale flow that incorporates viscous heat dissipation and compression work. Moreover, we demonstrated that viscous heat dissipation and compression work can promote the convection heat transfer and increase the number of vortexes, which is crucial for the microscale flow and therefore should be considered. These findings are crucial, and the model constructed in this study will be useful in promoting the development of microfluidic systems

ACKNOWLEDGEMENTS

Project supported by the National Natural Science Foundation of China (Grant Nos. 51075243, 11672164) and Natural Science Foundation of Shandong Province, China (Grant No. ZR2014EEM033).

REFERENCES

[1] Yang, H.and Zhu Z., Numerical simulation of turbulent Rayleigh–Benard convection. International Communications in Heat and Mass Transfer, 2006, 33(2): p. 184-190.

[2] Pallares, J., Cuesta I.and Grau F.X., Laminar and turbulent Rayleigh–Bénard convection in a perfectly conducting cubical cavity, International Journal of Heat and Fluid Flow, 6// 2002, 23(3): p. 346-358.

[3] Zhou, Q.and Xia K.-Q., Physical and geometrical properties of thermal plumes in turbulent Rayleigh–Bénard convection. New Journal of Physics, 2010, 12(7): p. 075006.

[4] Sun, C., Cheung Y.-H.and Xia K.-Q., Experimental studies of the viscous boundary layer properties in turbulent Rayleigh–Bénard convection. Journal of Fluid Mechanics, 2008, 605(6): p. 79-113.

[5] Sharif, M.A.R.and Mohammad T.R., Natural convection in cavities with constant flux heating at the bottom wall and isothermal cooling from the sidewalls. International Journal of Thermal Sciences, 2005, 44(9): p. 865-878.

[6] Valencia, L., Pallares J., Cuesta I.and Grau F.X., Turbulent Rayleigh–Bénard convection of water in cubical cavities: A numerical and experimental study. International Journal of Heat and Mass Transfer, 2007, 50(15-16): p. 3203-3215.

[7] Kao, P.H., Chen Y.H.and Yang R.J., Simulations of the macroscopic and mesoscopic natural convection flows within rectangular cavities. International Journal of Heat and Mass Transfer, 2008, 51(15-16): p. 3776-3793.

[8] Kao, P.H., Chen Y.H.and Yang R.J., Simulations of the macroscopic and mesoscopic natural convection flows within rectangular cavities. International Journal of Heat and Mass Transfer, 2008, 51(15-16): p. 3776-3793.

[9] Chakraborty, S.and Chatterjee D., An enthalpy-based hybrid lattice-Boltzmann method for modelling solid-liquid phase transition in the presence of convective transport. Journal of Fluid Mechanics, 2007, 592(592): p. 155-175.

[10] He, X., Chen S.and Doolen G.D., A novel thermal model for the lattice Boltzmann method in incompressible limit. Journal of Computational Physics, Oct 10 1998, 146(1): p. 282-300.

[11] Partha, M.K., Murthy P.and Rajasekhar G.P., Effect of viscous dissipation on the mixed convection heat transfer from an exponentially stretching surface. Heat & Mass Transfer, 2005, 41(4): p. 360-366.

[12] Pantokratoras, A., Effect of viscous dissipation and pressure stress work in natural convection along a vertical isothermal plate. New results. International Journal of Heat & Mass Transfer, 2003, 46(25): p. 4979-4983.

[13] Alam, M.M., Alim M.and Chowdhury M.M., Effect of pressure stress work and viscous dissipation in natural convection flow along a vertical flat plate with heat conduction, Journal of Naval Architecture and Marine Engineering, 2006, 3(2): p. 69-76.

[14] Lelea, D., Cioabla A.E.and Mihon L., The micro-tube heat transfer and fluid flow of methanol. Annals of Daaam & Proceedings, 2010.

[15] Hung, L.H.and Yang J.Y., A coupled lattice Boltzmann model for thermal flows. Ima Journal of Applied Mathematics, 2011, 76(5): p. 774-789.

[16] Zhang, J., Lattice Boltzmann method for microfluidics: models and applications. Microfluidics & Nanofluidics, 2011, 10(1): p. 1-28.

[17] Zhang, J., Yan G., Shi X.and Dong Y., A lattice Boltzmann model for the compressible Euler equations with second-order accuracy. International Journal for Numerical Methods in Fluids, 2009, 60(1): p. 95-117.

[18] Yan, Y.Y., Zu Y.Q.and Dong B., LBM, a useful tool for mesoscale modelling of single-phase and multiphase flow. Applied Thermal Engineering, 2011, 31(5): p. 649-655.

[19] Kao, P.H., Chen Y.H.and Yang R.J., Simulations of the macroscopic and mesoscopic natural convection flows within rectangular cavities. International Journal of Heat & Mass Transfer, 2008, 51(15): p. 3776-3793.

[20] Li, Q., Luo K.H., He Y.L., Gao Y.J.and Tao W.Q., Coupling lattice Boltzmann model for simulation of thermal flows on standard lattices. Physical Review E, 2012, 85(1): p. 016710-016716.

[21] Wang, J., Wang D., Lallemand P.and Luo L.S., Lattice Boltzmann simulations of thermal convective flows in two dimensions. Computers & Mathematics with Applications, 2013, 65(2): p. 262-286.

[22] Lallemand, P.and Luo L.S., Theory of the lattice Boltzmann method: acoustic and thermal properties in two and three dimensions. Physical Review E, 2003, 68(2): p. 036706.

[23] Mai, H.-C., Lin K.-H., Yang C.-H.and Lin C.-A., A thermal lattice Boltzmann model for flows with viscous heat dissipation, Computer Modeling in Engineering & Sciences(CMES), 2010, 61(1): p. 45-62.

[24] Guo, Y.L., Xu H.H., Shen S.Q.and Wei L., Nanofluid Raleigh-Benard convection in rectangular cavity: Simulation with lattice Boltzmann method. Acta Physica Sinica, 2013, 62(14): p. 1691-1702.

[25] Guo, Z., Zheng C., Shi B.and Zhao T.S., Thermal lattice Boltzmann equation for low Mach number flows: Decoupling model. Physical Review E, Mar 2007, 75(3).

[26] Liu, F.F., Wei, S.S., Wei, C.Z., Ren, X.F., Coupling double-distribution-function thermal lattice Boltzmann method based on the total energy type, Acta Physica Sinica, 2015, 64(15).

[27] Kim, B.J., Lee J.H.and Kim K.D., Rayleigh–Taylor instability for thin viscous gas films: Application to critical heat flux and minimum film boiling. International Journal of Heat & Mass Transfer, Jan 2015, 80: p. 150-158.

[28] Noghrehabadi, A., Izadpanahi E.and Ghalambaz M., Analyze of fluid flow and heat transfer of nanofluids over a stretching sheet near the extrusion slit. Computers & Fluids, Sep 1 2014, 100: p. 227-236.

[29] Kanna, P.R., Taler J., Anbumalar V., Kumar A.V.S., Pushparaj A.and Christopher D.S., Conjugate Heat Transfer from Sudden Expansion Using Nanofluid, Numerical Heat Transfer Part a-Applications, Jan 2 2015, 67(1): p. 75-99.